Direct attachment of well-aligned single-walled carbon nanotube architectures to silicon (100) surfaces: a simple approach for device assembly.

Jingxian Yu, Joseph G. Shapter, Jamie S. Quinton, Martin R. Johnston and David A. Beattie

Phys. Chem. Chem. Phys., 2007, 9, 510-520
DOI: 10.1039/B615096A

Direct attachment of well-aligned single-walled carbon nanotube architectures to silicon (100) surfaces: a simple approach for device assembly†

Jingxian Yu,[a] Joseph G. Shapter,*[a] Jamie S. Quinton,[a] Martin R. Johnston[a] and David A. Beattie[b]

Received 17th October 2006, Accepted 14th November 2006
First published as an Advance Article on the web 1st December 2006
DOI: 10.1039/b615096a

A new approach for the attachment of vertically-aligned shortened carbon nanotube architectures to a silicon (100) substrate by chemical anchoring directly to the surface has been demonstrated for the first time. The ordered assembly of single-walled carbon nanotubes (SWCNTs) was accomplished by hydroxylating the silicon surface followed by a condensation reaction with carboxylic acid functionalised SWCNTs. This new nanostructure has been characterised by X-ray photoelectron, Raman and Fourier transform infrared (FTIR) spectroscopy as well as scanning electron and atomic force microscopy. The assembly behaviour of SWCNTs onto the silicon surface shows a fast initial step producing isolated functionalised carbon nanotubes or nanotube bundles anchored to the silicon surface followed by a slower step where the adsorbed nanotubes grow into larger aggregates *via* van der Waals interactions between adsorbed and solvated nanotubes. The electrochemical and optical properties of the SWCNTs directly attached to silicon have also been investigated. These new nanostructures are excellent electrochemical electrodes. They also fluoresce in the wavelength range 650–800 nm. The successful attachment of the SWCNTs directly to silicon provides a simple, new avenue for fabrication and development of silicon-based nanoelectronic, nano-optoelectronic and sensing devices. Compared to existing techniques, this new approach has several advantages including low operating temperature, low cost and the possibility of further modification.

Introduction

Single-walled carbon nanotubes (SWCNTs) are elongated members of the fullerene family.[1,2] These one-dimensional molecular structures have recently become the focus of intense multidisciplinary study due to their unique structure, chirality-dependent conductivity, high mechanical strength and good chemical stability. These properties make carbon nanotubes excellent candidates for electron field emission sources,[3–6] scanning probe tips,[7–9] nanoelectronic devices,[10–15] energy storage devices[16–18] and actuators,[19] as well as chemical and biochemical sensors.[20–22] However, most of these potential applications require surface-mounted aligned carbon nanotube arrays grown with large-scale control of location and orientation.[23–25] In this regard, many efforts have been undertaken to fabricate highly oriented carbon nanotubes on device surfaces based on direct growth by chemical vapor deposition and self-assembling techniques.[4,5,23,26,27]

The direct patterned growth of aligned carbon nanotube arrays has been widely explored and successfully developed using chemical vapour deposition techniques. However, these methods have limitations with regard to large-scale applications because of the high growth temperature required,[4,26] poor adhesion between nanotubes and substrates,[5] success only for multi-walled carbon nanotubes[28] and the closed ends of carbon nanotubes.[5] Clearly, the high growth temperature makes positioning carbon nanotubes onto temperature sensitive substrates such as integrated circuit (ICs) impossible. In addition, poor adhesion results in long term reliability issues and high contact resistances.[5] Due to the capped ends of the nanotubes, further chemical modification will be difficult because continued processing of surface-mounted nanotubes may have a detrimental effect on the substrate itself.

Several methods have been developed for alkanethiol self-assembled monolayer (SAM) immobilisation onto metal surfaces and these have proved to be particularly powerful for SWCNT integration at low temperature.[23,27–35] However, their widespread technological application is uncertain due to issues related to the long-term stability of alkanethiols on gold surfaces. Dynamic studies of alkanethiols on gold surfaces have revealed several serious disadvantages in the thiol–gold chemistry. Of particular concern is thermal instability,[36,37] the influence of UV photoxidation,[38] evidence of changing structures over time,[37,38] instability in solution, gold etching and adsorbate–solution interchange.[39] Critical evidence of the maturation of alkanethiol SAMs films has shown that over a period of several months in air, dramatic changes

[a] *School of Chemistry, Physics and Earth Sciences, Flinders University, Bedford Park, SA 5042, Australia. E-mail: Joe.shapter@flinders.edu.au; Tel: +61 8 82012005*
[b] *Ian Wark Research Institute, University of South Australia, Mawson Lakes, SA 5095, Australia*
† The HTML version of this article has been enhanced with colour images.

occur in both the film structure and integrity due to oxidation processes.[37,38]

It is for these reasons that recent attention has been focused on the covalent attachment of carbon nanotubes to surfaces. For example, Jung *et al.*[6,22,40] has reported a novel method for producing high density carbon nanotube arrays through the formation of an amine terminated surface by treatment of a glass surface with an aminosiloxane followed by subsequent attachment of shortened carbon nanotubes *via* a condensation reaction between amine and carboxylic acid groups. These SWCNT layers have excellent surface adhesion because of their strong chemical bonding to the substrate. A disadvantage of this approach is the presence of the intervening SAMs which is an impediment in situations where electron transduction to the substrate is desirable.

In view of the importance of silicon as the primary semiconductor material in modern microelectronic devices, efforts to control its electronic properties and to tailor the chemical and physical characteristics of its surface are of major importance. We have previously reported the preparation of well-aligned carbon nanotube arrays on silicon (100) surfaces by reaction of a hydride-terminated silicon (100) with ethyl undecylenate to give SAMs that were linked by stable silicon–carbon covalent bonds.[41] The ester terminus of the monolayer was subsequently converted to an alcohol whereupon shortened carbon nanotubes were covalently attached using carbodiimide coupling. However, the presence of the SAM of organic material is expected to hinder electron transport between carbon nanotubes and the underlying silicon substrate. In addition, the deformation and distortion of the self-assembled molecules will give rise to non-alignment of carbon nanotube layer.

Thus we have been actively seeking methods to covalently attach carbon nanotubes to silicon without the use of intermediate molecules and this led us to hydroxyl terminated silicon as a potential substrate. The properties of hydroxyl terminated silicon are well known[42,43] and a standard procedure has already been established for its preparation.[44,45] The purpose of this paper is to demonstrate for the first time the attachment of shortened carbon nanotubes onto a silicon (100) substrate by direct chemical anchoring to produce a vertically aligned architecture. This is achieved by a condensation reaction between surface hydroxyl groups and carboxylic acid groups on the carbon nanotube. The preparation of the SWCNTs directly attached to a silicon surface was characterised using X-ray photoelectron (XPS) and Raman spectroscopies, Fourier transform infrared spectroscopy (FTIR), atomic force microscopy (AFM) and scanning electron microscopy (SEM) whereupon the formation mechanisms of nanotube arrays and their resultant electrochemistry and optical properties can be studied unambiguously.

Experimental

Preparation of SWCNTs directly attached to silicon (100)

Fig. 1 shows the schematic representation of the preparation of SWCNTs directly attached to silicon. Highly boron doped p-type silicon (100) wafers (0.5 mm thickness, 1 mΩ cm resistivity and polished on one side) were purchased from Virginia Semiconductor, Inc. USA. The surfaces (0.5 × 0.5 cm^2 size) were ultrasonically cleaned in acetone (99.5%, Merck) for 30 s and flushed with copious amounts of Milli Q water (18 MΩ cm). Subsequently the silicon pieces were immersed first into a 1 : 1 : 5 mixture of 30% NH_4OH (Sigma-Aldrich), 30% H_2O_2 (Sigma-Aldrich) and Milli Q water (18 MΩ cm) for 15 min at 80 °C, followed by immersion into a 1 : 1 : 5 mixture of 36% HCl (Ajax Finechem), 30% H_2O_2 (Sigma-Aldrich) and Milli Q water (18 MΩ cm) for 15 min at 80 °C.[44] The hydroxyl terminated silicon was incubated in a DMSO (99.9%, ACS Spectrophotometric Grade, Sigma-Aldrich) solution containing both 0.1 mg mL^{-1} dicyclohexyl carbodiimide (DCC, 99%, Aldrich) and 0.12 mg mL^{-1} functionalised carbon nanotubes. The nanotubes are RFP-SWCNT from Carbon Solutions, Inc. USA cut for 8 h in mixed acid as described previously[27,41] and suspended in DMSO. The silicon substrates are exposed to the nanotube solution for different exposure times to give carbon nanotubes directly attached to silicon surfaces. After exposure, the samples are rinsed in copious amounts of acetone to remove any unbound reagents.

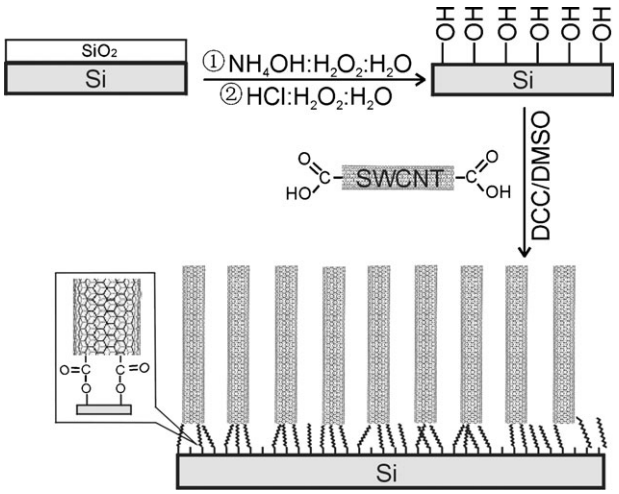

Fig. 1 Schematic representation of the preparation of SWCNTs directly attached to silicon.

X-Ray photoelectron spectroscopy measurements

X-Ray photoelectron spectra were obtained using an Axis Ultra (Kratos Analytical, UK) XPS spectrometer equipped with an Al Kα source (1486.6 eV). The take-off angle for detection was nominally 90° from the surface. The pressure in the analysis chamber was less than 5 × 10^{-8} Torr during analysis. Spectra of the Si_{2p} (90–110 eV binding energy), C_{1s} (276–296 eV binding energy) regions and survey scans (0–1000 eV binding energy) were recorded. The analysis of high-resolution XPS peaks was performed using the computer aided surface analysis for X-ray photoelectron spectroscopy (Casa XPS) software with 30% Lorentzian and 70% Gaussian functions and using a Shirley baseline subtraction. In the atomic analysis, atomic sensitivity factors of 0.296, 0.711 and 0.283 were used for carbon (1s), oxygen (1s) and silicon (2p), respectively.[46]

Atomic force microscopy

Atomic force microscope tapping mode images were taken in air with a multi-mode head and Nanoscope IV controller (Digital Instruments, Veeco, Santa Barbara). Commercially available silicon cantilevers (FESP-ESP series, Veeco probes, Santa Barbara) with fundamental resonance frequency between 70–85 KHz were used. Topographic (height) and amplitude images were obtained simultaneously at a scan rate of 1 Hz with the parameters of set point, amplitude, scan size, and feedback control optimised for each sample. All images presented represent background subtracted data using the 'flatten' feature in the Digital Instruments software.

Scanning electron microscopy

Scanning electron microscope images were obtained with a Philips XL30 field emission scanning electron microscope, with an accelerating voltage as indicated in each image (Acc V). Prior to the SEM imaging, the sample was sputter-coated with a 2 nm thick platinum layer. All images were scanned using the slowest-scan mode for improved clarity.

Fourier transform infrared spectroscopy

Silicon (100) plates (15 mm × 55 mm size) were placed carefully with the polished side of the wafer facing down in direct contact with the flat germanium ATR crystal (50 mm × 10 mm × 3 mm size, 45° bevel angle). The analysis angle was set to 30° for the variable angle horizontal ATR accessory (Pike Technologies, Inc., USA). The number of reflections in the crystal is 28. FTIR spectra were measured using a Bio-RAD FTS-40A spectrometer equipped with a mercury cadmium telluride (MCT) detector cooled with liquid nitrogen. All spectra were recorded by integrating 128 interferograms in the wavenumber range 1000–4000 cm^{-1} with a resolution 2 cm^{-1}. Reference spectra were obtained using a hydroxyl terminated silicon (100) surface. The germanium crystal was cleaned with neat 2-butanone before every experiment and the ATR accessory was purged with high purity N_2 during data acquisition.

Raman spectroscopy

A commercial Raman microscope (Renishaw Ramascope System 1000) was used to collect Raman scattered light. The system consists of a single spectrograph fitted with holographic notch filters and a Peltier cooled CCD detector upon which the Raman spectrum is dispersed. The spectrograph is coupled to a Leica microscope (DMLM) with computer controlled sample stage, rigidly fixed to the spectrograph baseplate. The spectrometer has a maximum lateral resolution of 2 μm and depth resolution of 2 mm; however, the effective field of view was increased to allow signal collection from a larger area. The spectrometer is equipped with three lasers for use in the standard normal incidence sampling geometry: 532, 633, and 785 nm. The two visible wavelengths deliver around 5 mW of power to the sample, whereas the 785 nm laser delivers around 100 mW. The 785 nm laser (Renishaw-badged compact diode laser) was used for the spectra reported in this work, and was focused onto the sample using a ×50 objective (Leica, NA = 0.75). The 785 nm laser produces a line focus at the sample, increasing the area analysed during acquisition. Calibration of the instrument was checked with the emission lines of a neon lamp.

Fluorescence spectroscopy

A Cary Eclipse fluorescence spectrometer equipped with a solid sample holder accessory was used to investigate the fluorescence properties of the carbon nanotube modified silicon surface. Hydroxyl terminated silicon (100) was used as a reference surface. The fluorescence emission spectra were obtained by exciting at 440, 473 and 510 nm, respectively, with both excitation and emission slit widths of 20 nm.

Electrochemical measurements

All electrochemical experiments were carried out in a specially designed electrochemical cell shown in Fig. 2. The hydroxyl terminated silicon or the well-aligned carbon nanotube modified silicon were used as the working electrode. The electrical contact to the working electrode was maintained by scratching the unpolished side of the wafer with a SiC crystal and adhering freshly polished aluminium foil to the scratched side. A polypropylene pipette (~1 mL) tip, containing a platinum wire counter electrode, a bare silver wire (Ag^+/Ag) reference electrode and electrolyte solution, was pressed down against the silicon samples. 0.1 mol L^{-1} TBAP (98%, tetrabutylammomium perchlorate, Fluka)–CH_3CN (Isocratic HPLC grade, Scharlau Chemie) solutions with and without 0.1 mmol L^{-1} ferrocene (98%, Aldrich-Sigma) were used as the electrolyte solutions. Because a very small working electrode area is involved, the RC time constant of the electrochemical cell can be shortened considerably so that the fast kinetic events can be accurately measured. Compared to the electrochemical cell reported by Bocian *et al.*,[47] the electrochemical cell described here has some distinct advantages, such as the simplicity and low fabrication costs as well as the application of a three electrode system as opposed to the two electrode

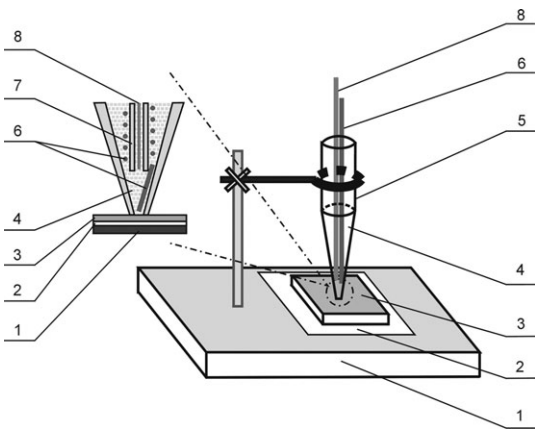

Fig. 2 Schematic diagram of the specially designed electrochemical cell. (1) Modified retort stand, (2) aluminium foil, (3) silicon working electrode, (4) organic electrolyte, (5) polypropylene pipette, (6) platinum wire winding counter electrode, (7) PTFE tubing for insulation between the silver and platinum wire, (8) bare silver wire reference electrode.

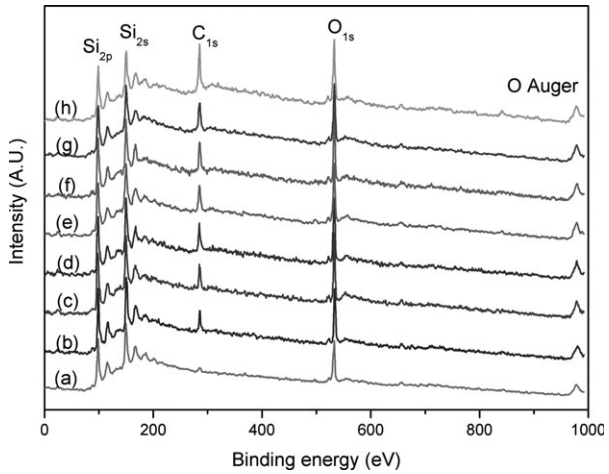

Fig. 3 A series of X-ray photoelectron survey spectra for carbon nanotubes directly attached to silicon (100) surfaces after hydroxyl terminated silicon surfaces were immersed in a functionalised carbon nanotubes–DCC–DMSO suspension for different exposure times at 80 °C. All spectra are normalised relative to the intensity of the Si_{2p} peak. (a) 0, (b) 1.3, (3) 10.5, (d) 20, (e) 40, (f) 60, (g) 80 and (h) 100 h.

system used in ref. 45. All electrochemical experiments were performed inside a dry-box filled with high purity N_2 using a BAS 100B Electrochemical Analyser at room temperature.

Results and discussion

The steps involved in fabricating the aligned nanotube arrays on silicon surfaces are illustrated in Fig. 1. Firstly the silicon oxide layer on the silicon surface is removed in a two step process to give a hydroxyl terminated silicon surface. This surface is reacted with functionalised nanotubes which have been activated by incubation in DCC which converts carboxylic acid moieties on the ends and defects on the wall of the SWNTs to carbodiimides. The carbodiimides are susceptible to nucleophilic attack from the alcohol terminated silicon to give an ester bond. The end result is covalent attachment of the SWCNTs directly to the substrate. In the ideal case, the SWCNTs will only attach from their ends to give aligned carbon nanotube arrays. The experiments described herein probe the physical, chemical and electronic structure of the newly formed interface which sees SWCNTs directly attached to silicon.

X-Ray photoelectron spectra

The attachment of shortened nanotubes to the surface was achieved by immersing hydroxyl terminated silicon in a suspension of DCC and functionalised nanotubes in DMSO at 80 °C for various times. Shown in Fig. 3 are a series of X-ray photoelectron survey spectra for surfaces exposed to the nanotube solutions for various lengths of time.

In the case of the parent hydroxyl terminated silicon (100) surface (curve a in Fig. 3), Si 2s, Si 2p, O 1s and oxygen Auger peaks are observed at binding energies of 99.5, 151.5, 531.6 and 979.5 eV, respectively. After being exposed to the functionalised carbon nanotubes for different times, a peak at binding energy 285 eV appears which is due to the presence of carbon. In addition, the size of this C_{1s} peak increases with increasing exposure time indicating an increased amount of carbon on the surface. The absence of N 1s peaks for any exposure time indicates the complete removal of DCC in the post exposure rinse.

Fig. 4 depicts typical high resolution C 1s and Si 2p X-ray photoelectron spectra of a silicon sample with SWCNTs directly attached. From the Si 2p spectrum (Fig. 4a), two peaks at binding energies of 102.7 and 99.0 eV are observed. The former is assigned to the oxidised or hydroxylated silicon surface. The peak at 99.0 eV is from the substrate, which is deconvoluted into peaks at 99.5 and 98.9 eV. Typically the peak at 99.5 eV is assigned to Si $2p_{1/2}$ while the peak at 98.9 eV is assigned to Si $2p_{3/2}$.[48,49] The C 1s peak (shown in Fig. 4b) exhibits five distinct components; namely at 284.6, 286.1, 287.4, 289.1 and 290.7 eV according to the deconvolution using Casa XPS software. In accordance with XPS peak assignments for functionalised carbon nanotubes previously adopted by Okpalugo *et al.*,[50] the following bonds were assigned: 284.6 eV (sp^2 C=C/sp^3 C–C), 286.1 eV (C–O), 287.4 eV (C=O) and 289.1 eV (–COO). The peak at 290.7

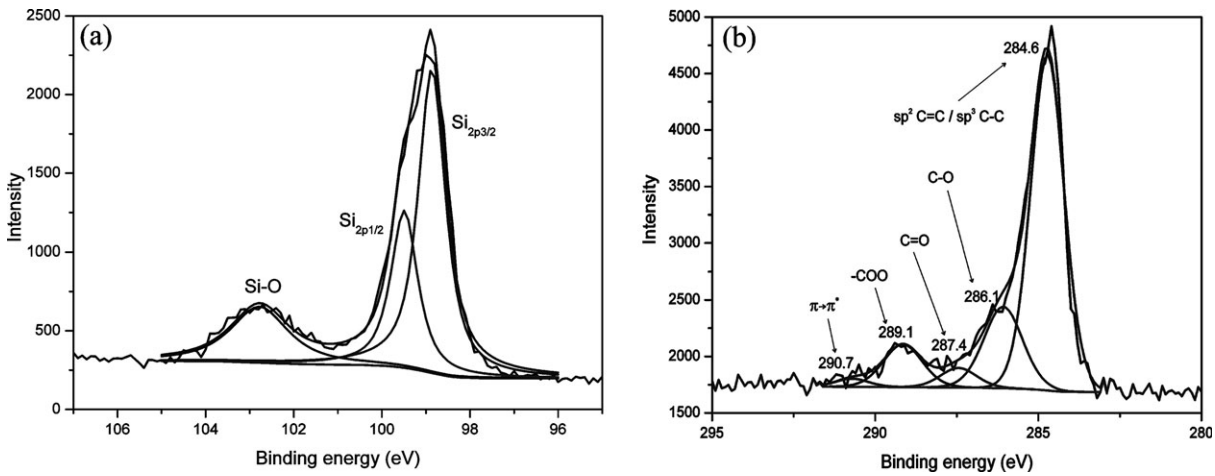

Fig. 4 High resolution (a) Si_{2p} and (b) C_{1s} X-ray photoelectron spectra for the SWCNTs directly attached to silicon with 24 h exposure time at 80 °C.

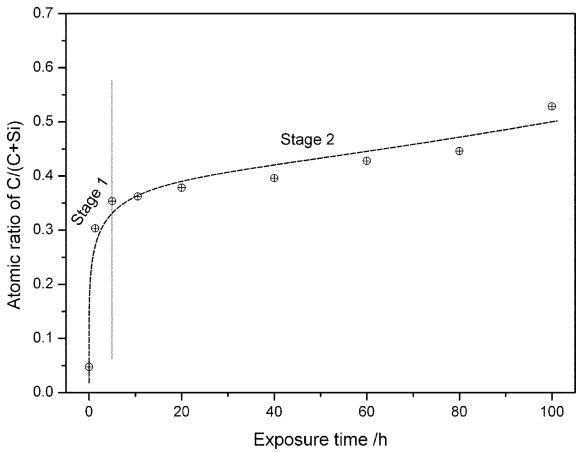

Fig. 5 Dependence of the atomic ratio of C : (C + Si) on exposure time determined from XPS data.

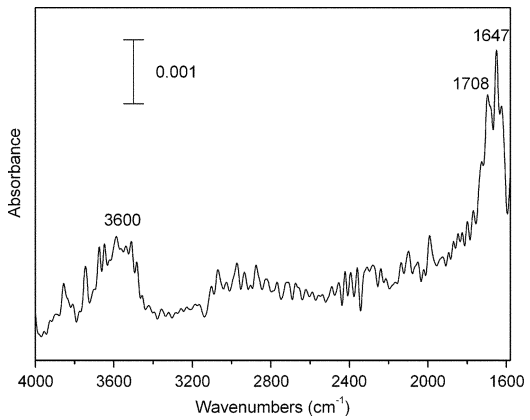

Fig. 6 Infrared spectrum for the SWCNTs directly attached to a silicon (100) surface, where the hydroxyl terminated silicon was exposed to a SWCNT–DMSO suspension for 24 h at 80 °C.

eV is assigned to the π band shake-up satellite for C 1s in shortened carbon nanotubes, which involves the energy of π → π* transition.[46,50] This shake-up transition is due to the fact that carbon nanotubes have been functionalised using an oxidising mixture of strong acids before the surface attachment and hence they still have various oxygen containing functional groups at their free ends.

Based on the X-ray photoelectron survey spectra shown in Fig. 3, the peak area ratio of C : (C + Si) has been calculated, where all 5 components of C 1s and the substrate Si 2p peak (at 99 eV) were involved in area calculation (after correction for elemental sensitivity). The intensity of C 1s in the XPS spectrum is indicative of the amount of SWCNTs that are present on the silicon substrate and hence it can be exploited to investigate the assembly behaviour of SWCNTs. Fig. 5 demonstrates the C : (C + Si) ratio dependence on the time that the substrate is exposed to the nanotube solution. The line in Fig. 5 is not a fit to the data, but rather is included to simply guide the eye. It is apparent that the ratio of C : (C + Si) increases sharply in the first 5 h and then slowly with exposure time, which indicates two different assembly behaviours. When Diao and Liu[28] investigated the assembly kinetics of SWCNTs on alkanethiol-modified gold surfaces, they reported a similar trend based on the dependence of the G-line intensity in polarised Raman spectra on the assembly time. Compared to their results, our analysis of the second stage kinetics (as per Fig. 5) for the assembly of SWCNTs onto hydroxyl terminated silicon exhibits a slightly faster rate. Moreover, even at long exposure times (100 h), the assembly process had not reached 'saturation' and further attachment at longer exposures still appears to be possible.

A likely explanation for the observed adsorption behaviour lies in the fact that the assembly of SWCNTs in the first stage of the process is controlled by the surface condensation reaction. In detail, isolated functionalised carbon nanotubes or nanotube bundles anchor to the silicon surface separately. After the stage of attachment through chemisorption, the assembly of SWCNTs is driven by van der Waals interactions between the hydrophobic side walls of the anchored nanotubes and those still in solution to form larger aggregates. At higher coverages, it would be expected that steric hindrance of anchored SWCNTs will limit access to the free SWCNTs in the suspension[28] hence slowing growth. This is the second stage of the observed growth process.

Infrared spectroscopy

Infrared spectroscopy has been used to verify and follow specific chemical functionalities. The spectrum for the SWCNTs directly attached to the silicon surface is presented in Fig. 6. IR measurements (and associated peak assignments) of functionalised nanotubes have been reported previously.[51,52] Of particular relevance is the peak at 1708 cm^{-1} (attributed to ν(C═O) in the functionalised nanotubes) and the peak at 1647 cm^{-1} (attributed to quinone type units along the side walls of the nanotubes).[51,52] The peak due to ν(C═O) in the carboxylic acid groups is observed at 1720 cm^{-1} for unattached nanotubes.[53] Upon adsorption onto the surface the ν(C═O) peak shifts to lower wavenumbers (1720 cm^{-1} *versus* 1708 cm^{-1}) in the adsorbed state. This shift has been observed previously and is attributed to increased hydrogen bonding.[51,54] The peak observed at 3600 cm^{-1} is due to the OH groups of the carboxylic acid groups on the unreacted end of the nanotubes. The OH stretch observed at 3600 cm^{-1} is very broad, most likely due to hydrogen bonding. After the condensation of the nanotubes into bundles on hydroxyl terminated silicon, it is not surprising to see an increase in intermolecular interactions leading to increased hydrogen bonding and hence a broad peak.

Raman spectroscopy

Fig. 7 shows typical Raman spectra of the hydroxyl terminated silicon and SWCNTs directly attached to silicon (prepared with 24 h exposure at 80 °C). For the hydroxyl terminated silicon, only a broad band at 950 cm^{-1}, which is due to bulk silicon, was observed. In contrast, the SWCNTs directly attached to silicon spectrum has two resonance-enhanced Raman bands present; the so-called 'D' band at 1314 cm^{-1} and so-called 'G' band at 1595 cm^{-1}. The difference spectrum (shown as curve (c) in Fig. 7) highlights these bands.

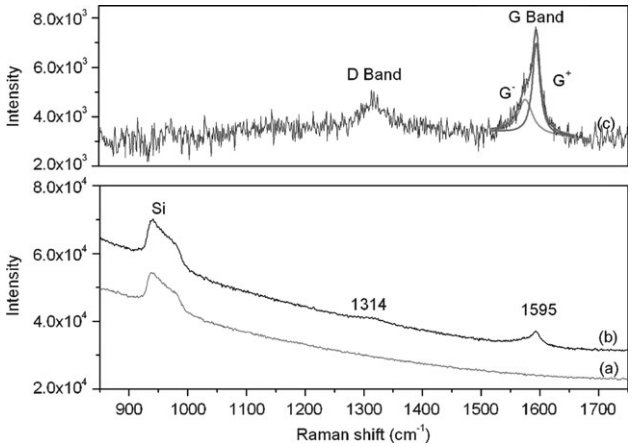

Fig. 7 Typical Raman spectra using a $\lambda = 785$ nm laser line for hydroxyl terminated silicon (a) and SWCNTs directly attached to silicon (b), where the SWCNTs directly attached to silicon was prepared by exposure in SWCNTs–DMSO suspension for 24 h at 80 °C. Curve (c) is the difference spectrum obtained by subtracting curve (a) from curve (b).

The two peaks appearing in spectrum (c) are well-known as the tangential band (G band) and the disorder-induced band (D band) for SWCNTs.[55–58] The G band provides information about the chirality of SWCNTs, where different chiralities lead to either semiconducting or metallic nanotubes. The G band can be further deconvoluted into two peaks, G^+ and G^-, using Lorentzian peaks. The Raman shifts of these peaks are measured to be 1595 and 1570 cm^{-1}, respectively. The laser excitation energy (E_{laser} 1.58 eV $\lambda = 785$ nm) employed in these experiments lies directly between the dominant excitation energies for both metallic (1.7 eV $\leq E_{laser} \leq$ 1.9 eV) and semiconducting (above 2.2 eV or below 1.5 eV)[57] nanotubes. It would be expected that both types of nanotubes could be identified if they were present.

Analysis of the peak areas reveals that the G^+ peak area is slightly greater than that of the G^- peak, by approximately 10%. Although the linewidth of the G^- peak is about 33 cm^{-1}, which is broader than that of the G^+ peak, the G^- peak does not have a Breit–Wigner–Fano (BWF) lineshape (broad and asymmetric). This indicates that the carbon nanotubes attached to the silicon surface in this work exhibit considerable semiconducting character.[55] RFP-SWCNTs produced by an electric arc technique are generally a mixture of metallic and semiconducting nanotubes.[59] Indeed, for the raw material used in this work, the G^+/G^- ratio is found to be 0.73 indicating a greater amount of metallic nanotubes in the starting material than in the attached nanotubes. The increase in semiconducting nature of the attached nanotubes must be due to the fact that the RFP-SWCNTs were exposed to concentrated mixture of 3 : 1 H_2SO_4–HNO_3 for 8 h before they were reacted with the hydroxyl terminated silicon surface. This oxidising process will create many defects in the carbon lattice of the nanotube's sidewalls which will lead to a greater semiconducting character of the SWCNTs that have been subjected to chemical oxidation. As these nanotubes are used in the attachment reaction, the observed increased semiconducting character of the attached nanotubes is exactly what is expected.

The 'D' band in the Raman spectrum, on the other hand, provides information on nanotube purity and the integrity (*i.e.* how ordered) of the nanotube's graphene structure, as the size of the peak gives an indication of the amount of amorphous and poorly organised material present in the sample.[55,58] Previous reports involving the study of the relative amounts of amorphous and ill-organised carbon have used the peak area ratio of D/G using the total G band intensity. In Fig. 7c, the ratio of D/G was calculated to be 0.31. The D/G ratio observed for the unmodified nanotubes used as the starting material in these experiments was measured to be 0.08. In other work in the literature, ratios as small as 0.01 for isolated as-prepared SWCNTs,[55] and 0.1 for vertically-aligned SWNCT arrays prepared by molecular beam-controlled nucleation and growth[60] have been reported. The larger D/G value for the SWCNT nanostructure in this work can be attributed to the defects on the sidewall of the carbon nanotubes caused by the cutting process. These defects in effect disrupt the ordering of the carbon atoms in the nanotubes and hence lead to increased intensity in the D band.

Atomic force and scanning electron microscopy

Microscopy has been used to probe the morphology of the surface at each step of the fabrication process. Fig. 8 shows tapping mode AFM images as well as an SEM image of silicon substrates exposed to the SWCNTs solution for various exposure times. Before attachment of functionalised carbon nanotubes, the hydroxyl terminated silicon pieces are observed to be very flat surfaces. However, after the surface condensation reaction, protrusions are clearly observed in AFM images (Fig. 8a–c). Similar carbon nanotube islands are also observed in SEM images (Fig. 8d). At the short exposure times (*e.g.* 2 h, shown in Fig. 8a), well separated carbon nanotube islands can be seen separated by large areas of bare silicon surface. As the exposure time increases, both the number and size of carbon nanotube islands appear to increase. The coverage for different exposure times has been measured to be 36% after 2 h exposure; 85% after 20 h exposure and 90% after 100 h exposure using AFM data, and 33.4% after 2 h exposure using SEM data. The coverage obtained by AFM for 2 h exposure is in good agreement with that obtained by SEM. The average island diameters are ~95 nm for 2 h exposure; ~110 nm for 20 h exposure; and ~140 nm for 100 h exposure; as measured *via* AFM. When determined from the SEM data for the 2 h sample, the average island diameter is found to be ~67 nm. The observed increase in diameter as a function of exposure time is consistent with the formation of nanotube bundles. Moreover, as one would expect, the average diameter at a given exposure when determined from AFM images is larger than that from SEM, due to tip convolution effects that are inherent in the AFM technique. The average (and maximum) height was also measured *via* AFM, and found to be 22.9 nm (41.1 nm) after 2 h exposure; 29.8 nm (72.0 nm) after 20 h exposure; and 35.5 nm (101.5 nm) after 100 h. Again, the trend shows an increasing height with reaction time, as one would expect. The separated SWCNTs islands

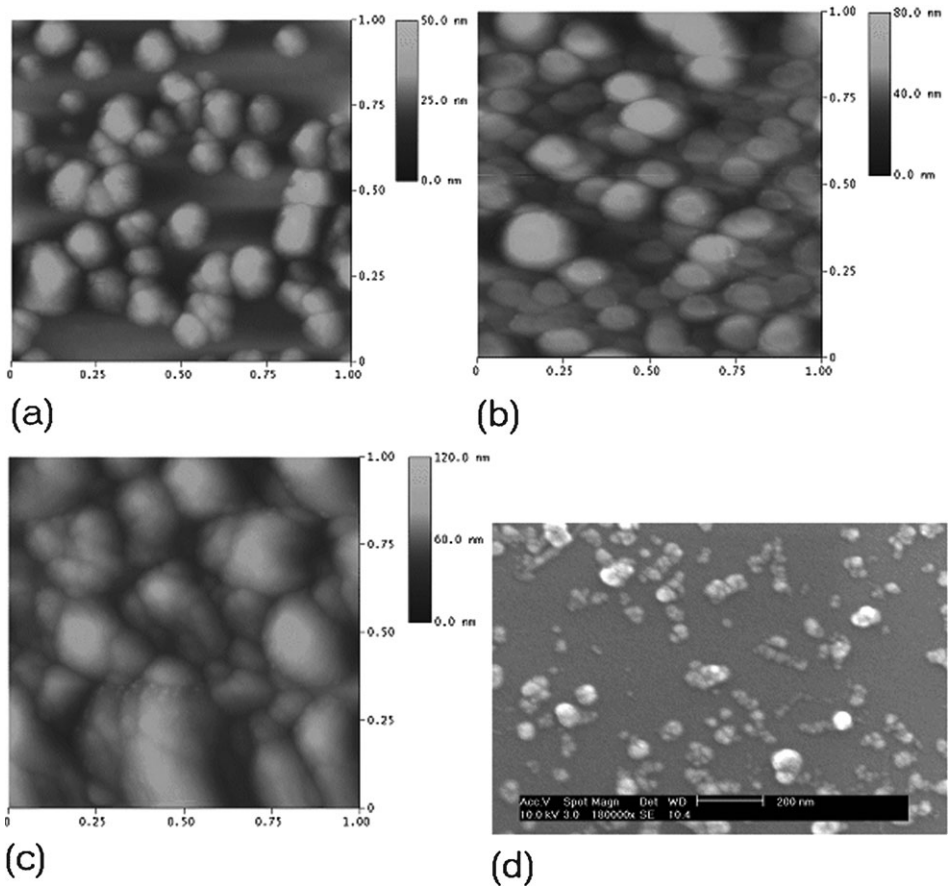

Fig. 8 Tapping mode AFM and SEM images for the SWCNTs directly attached to silicon surfaces after different exposure times at 80 °C, where (a) 2, (b) 20 and (c) 100 h exposure time images were obtained by AFM with scan size 1 μm × 1 μm, and (d) 2 h exposure time obtained by SEM (scale bar shown in image).

shown in Fig. 8a and d support the island growth model presented earlier.

In direct contrast to our earlier work using a SAM to attach nanotubes to silicon substrates, the AFM results presented here show very few nanotubes lying horizontally on the substrate.[41] This extra element of orientational control is governed by the hydrophilic nature of the hydroxylated substrate, which makes interactions with the hydrophobic side walls of the nanotubes very unfavourable. In the case of the SAM, the aliphatic section of the molecules seems to have given the surface enough hydrophobic character to allow sidewall interactions.

In order to quantitatively estimate the total 'volume' and thus the amount of nanotubes successfully attached to the surface, the product of AFM determined averages of coverage and height was calculated. This method is deemed more accurate than surface coverage alone as it best defines the total amount of material deposited. Fig. 9 shows the dependence of normalised AFM SWCNT amounts on exposure time. The observed growth is in good agreement with the results obtained by XPS (Fig. 3) further supporting the assembly mechanism of SWCNTs onto the silicon surface.

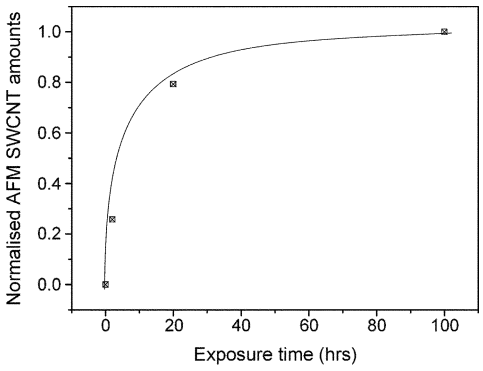

Fig. 9 The dependence of normalised AFM SWCNT amounts on exposure time, where AFM SWCNT amount is defined by the product of AFM surface coverage and average height of SWCNTs.

Fluorescence spectroscopy

Fluorescence spectroscopy was employed to further verify the successful attachment of SWCNTs. Following excitation at various wavelengths between 440–510 nm, SWCNTs directly attached to a silicon surface exhibit fluorescence in the wavelength range from 650–800 nm. The excitation spectrum for this nanostructure shows peaks at 442, 473, 513, 563 and 594 nm. Exciting the system at different wavelengths yields fluorescence shifted well to the red of the excitation wavelength. Fig. 10 shows the fluorescence emission spectra for

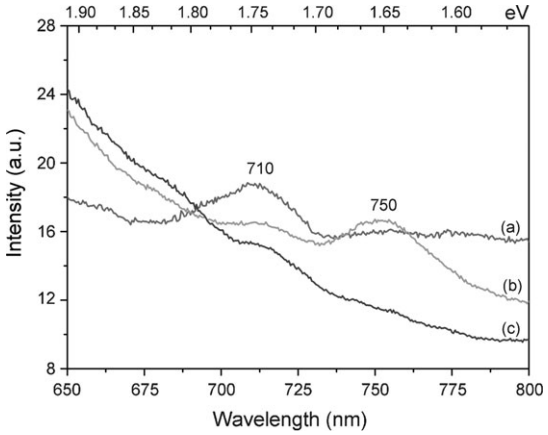

Fig. 10 Fluorescence emission spectra for SWCNT directly modified silicon when the surface was excited by different wavelengths, (a) 440, (b) 473 and (c) 510 nm.

SWCNTs directly attached to silicon when using different excitation wavelengths.

It is very apparent that the emission spectra show strong excitation wavelength dependence. In detail, when the surface was excited at 440 nm, only one emission peak at 710 nm (1.75 eV) was observed. However, when the surface was excited at 473 nm, a new emission peak at 750 nm (1.66 eV) is observed while the existing emission peak at 710 nm is reduced in intensity. Interestingly when the surface was excited at 510 nm, the emission peak at 750 nm disappears altogether and while the peak at 710 nm remains, it is quite small. The fluorescence linewidths of 710 nm (λ_{ex} = 440 nm) and 750 nm (λ_{ex} = 473 nm) are 26.1 nm (0.065 eV) and 23.4 nm (0.052 eV), respectively. No fluorescence is observed for unattached nanotubes while a small, continuous background fluorescence is observed for the bare hydroxylated substrate. The bare substrate is used as the reference in these experiments so the fluorescence observed for the nanostructure is over and above this.

To our knowledge, no similar observations of fluorescence emission have been reported for a SWCNT–silicon structure even though there are several examples of vertically-aligned SWCNT arrays.[5,60–63] Both emission peaks cannot be simply assigned to the silicon substrate because bulk crystalline silicon has a band gap of 1.1 eV and should result in luminescence in the near infrared region (~1100 nm). Additionally, the band gap fluorescence from individual semiconducting SWCNTs has been theoretically predicted and experimentally confirmed in the 800–1600 nm region of the near infrared.[64–67] However a further complicating issue is that the photoluminescence intensity is dramatically reduced by aggregation of isolated nanotubes.[64–66] In these experiments, the fact that SWCNTs bundle together even after 2 h of exposure has been shown using AFM and SEM. Moreover the linewidths of emission spectra should be approximately 10 nm (0.025 eV) if the fluorescence is from individual SWCNTs.[65,66] Both of the peak linewidths for SWCNTs directly attached to silicon are greater than this value, indicating that the attached SWCNTs exhibit a different mechanism than individual SWCNTs. In this case the fluorescence must be attributable to a combined effect involving the attached SWCNTs and silicon substrate.

The lack of emission from the separate components means that the observed fluorescence must be due to a feature of the newly created nanostructure. One possibility is the newly formed ester linkage. This seems unlikely as the observed shifts in fluorescence wavelengths for esters typically used in flow cytometry experiments is tens of nanometers.[68] Additionally, if the ester linkage did fluoresce one might expect some fluorescence from the carboxylic acid group of the cut nanotubes before surface attachment and this is not observed.

The large shift between the excitation wavelengths and the observed emission suggest that one species may be excited while a second is fluorescing. Indeed, there are a few cases of large shifts in the fluorochromes commercially available but these all involve conjugates of two quite different species[69]—one for excitation and one for emission. In the case of the silicon nanostructure formed in this work, it is thought that the nanotubes are excited but then strongly couple to the electronic states of the substrate, allowing an intersystem crossing of energy into the silicon band structure. Emission from porous silicon is well established since Canhan and Rowsell and Veinot[70,71] discovered that electrochemically etched porous silicon possessed remarkable optical properties. While emission from porous silicon can be observed over a wide range of wavelengths, the S band has peak intensity in the region where the emission in this work is observed.[72] Additionally, recent work has shown porous silicon emission spectra with peak intensities in the 650 nm region obtained using excitation between 400 and 450 nm.[73]

The nanostructure here physically resembles porous silicon to some extent as shown in Fig. 8. Observation of dramatically shifted fluorescence emission indicates a very strong coupling of the electronic states of the nanotubes and the substrate. In essence, the two components of the nanostructure seem to be coupled electronically to such an extent to appear much like one integrated structure. The electrochemistry results also confirm the strong coupling of the electronic states.

Electrochemistry

One of the end uses of these interfaces could be in the construction of sensors that will require the measurement of current. Some basic electrochemistry work was undertaken to probe the ability of the nanotube substrates to conduct electrons. Fig. 11 shows the cyclic voltammograms (CVs) using SWCNTs directly attached to silicon or the hydroxyl terminated silicon as the working electrode in 0.1 mmol L^{-1} ferrocene dissolved in 0.1 mol L^{-1} TBAP–CH_3CN solution as well as a CV using a SWCNTs directly attached to silicon working electrode in a TBAP–CH_3CN blank solution. For the SWCNTs directly attached to silicon in ferrocene–TBAP–CH_3CN solution shown in Fig. 11a, the potential was swept from 100 to 800 mV going in the anodic direction first. Clearly evident from Fig. 11a are distinct redox waves with anodic and cathodic peak positions at 474 and 596 mV, respectively. The oxidation of ferrocene to the stable ferricenium cation is a simple one-electron transfer reaction, in that

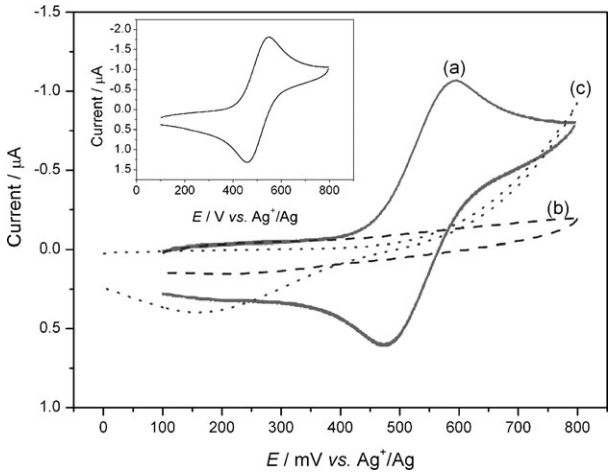

Fig. 11 Cyclic voltammograms using (a) SWCNTs directly attached to silicon working electrode and (c) hydroxyl terminated silicon working electrode in 0.1 mmol L^{-1} ferrocene dissolved in 0.1 mol L^{-1} TBAP–CH_3CN solution, and (b) SWCNTs directly attached to silicon working electrode in 0.1 mol L^{-1} TBAP–CH_3CN blank solution (b) at scan rate of 100 mV s^{-1}. The inset shows the cyclic voltammogram on a gold electrode in 0.1 mmol L^{-1} ferrocene dissolved in 0.1 mol L^{-1} TBAP–CH_3CN solution at scan rate 100 mV s^{-1}.

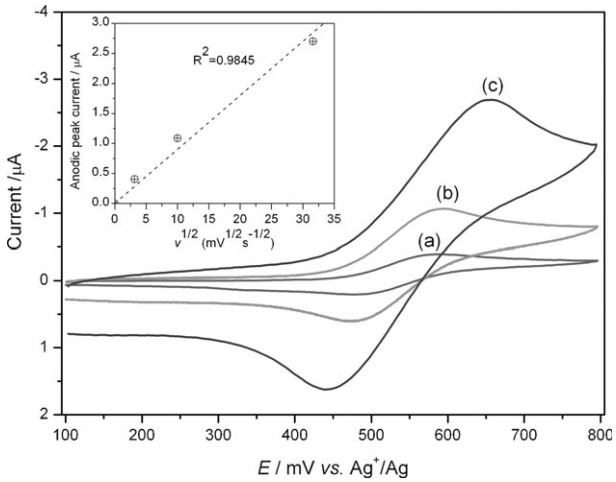

Fig. 12 Cyclic voltammograms using SWCNTs directly attached to silicon working electrodes in 0.1 mmol L^{-1} ferrocene dissolved in 0.1 mol L^{-1} TBAP–CH_3CN solution at different scan rates, (a) 10, (b) 100 and (c) 1000 mV s^{-1}. The inset shows the dependence of anodic peak current on the square root of scan rate.

there are no complications arising from adsorption or associated chemical reactions. The oxidation/reduction peak potentials on SWCNTs directly attached to silicon are comparable to those on a gold electrode in the same ferrocene–TBAP–CH_3CN solution (inset shown in Fig. 11). When the SWCNTs directly attached to silicon electrode was immersed in the blank solution without ferrocene, the CV looks very flat with only capacitive current observed. This result further proves that the redox waves shown in Fig. 11a are attributable to the oxidation/reduction of ferrocene in the solution.

In addition, the CVs on hydroxyl terminated silicon were measured and are shown in Fig. 11c. The potential was swept from 0–800 mV going in the anodic direction first. In this case, a broad reduction peak at 150 mV was observed but no obvious oxidation peak even under more positive switching potentials was seen. Compared to the CVs on hydroxyl terminated silicon, SWCNTs directly attached to silicon yields electrochemistry with much better reversibility and enhanced conductivity compared to the bare substrate.

Fig. 12 shows the CVs using a SWCNTs directly attached to silicon working electrode in 0.1 mmol L^{-1} ferrocene dissolved in 0.1 mol L^{-1} TBAP–CH_3CN solution at different scan rates. As expected, the oxidation/reduction current gets bigger with increasing scan rate. The inset shown in Fig. 12 shows the dependence of anodic peak current on the square root of scan rate. The straight line suggests that the oxidation/reduction process is controlled by semi-infinite linear diffusion of ferrocene to the interfacial reaction zone. At the same time, the peak-to-peak separation ΔE_p becomes larger with increasing scan rates, which is consistent with a quasi-reversible electrochemical reaction. ΔE_p was recorded at different scan rates (10–1000 mV s^{-1}). The electron transfer rate constants k_s were calculated from the dependence of the ΔE_p on the dimensionless kinetic parameter Ψ, according to the theory developed by Nicholson.[74,75] Assuming the diffusion coefficient for ferrocene in acetonitrile, D_R, is equal to that of ferricenium cation, D_o, and the transfer coefficient is $\alpha = 0.5$, the rate constants were calculated at different scan rates assuming $D_R = 2.4 \times 10^{-5}$ cm^2 s^{-1}.[76] The results are listed in Table 1. The average rate constant for SWCNTs directly attached to silicon in 0.1 mmol L^{-1} ferrocene dissolved in 0.1 mol L^{-1} TBAP–CH_3CN solution is 4.54×10^{-3} cm s^{-1}.

The rate constants reported herein may be compared to values reported in the literature for a variety of solid electrodes. Noel and co-workers[77] reported that the rate constants on platinum, glassy carbon and polypropylene composite graphite (CPP) electrodes in ferrocene–TBAP–CH_3CN solution were 5.1×10^{-3}, 4.5×10^{-3} and 3.3×10^{-3} cm s^{-1}, respectively which are of a similar value to those observed with the SWCNTs directly attached to silicon. In contrast to this, Swain and co-workers[78] reported rate constants on microcrystalline boron-doped diamond (BDD) and glassy carbon electrodes in ferrocene–TBAP–CH_3CN solution were 4.8×10^{-2} and 5.1×10^{-2} cm s^{-1}, respectively, which are about 10 times larger than those observed in this work. The exact reason for the difference using glassy carbon reported by Swain and Noel (a 10 fold difference) could be due to different experimental conditions such as the treatment of electrode surfaces and the purity of the solvent/electrolyte. In order to

Table 1 Calculation of electron transfer rate constants of 0.1 mmol L^{-1} ferrocene in 0.1 mol L^{-1} TBAP–CH_3CN solution on SWCNTs directly attached to silicon at different scan rates

Scan rate/mV s^{-1}	ΔE_p/mV	Ψ	k_s/cm s^{-1}
10	109	0.454	2.46×10^{-3}
100	122	0.344	5.89×10^{-3}
1000	217.6	0.097	5.26×10^{-3}
Average			4.54×10^{-3}

compare rate constants under the same experimental conditions, the rate constant on gold was estimated using peak separations[74] to be 1.32×10^{-2} cm s^{-1} at a scan rate of 100 mV s^{-1} based on the inset shown in Fig. 11. This value is 2–3 times larger than that on SWCNTs directly attached to silicon. Given this, the rate constant for the SWCNT surface is quite reasonable. The results indicate that SWCNTs directly attached to a silicon electrode possess a sufficient density of states to support relatively rapid electron transfer kinetics. This means that potential applications such as the fabrication and development of silicon-based electrochemical and bio-electrochemical sensors are certainly feasible.

Conclusions

This work successfully demonstrates a new approach for the fabrication of vertically-aligned shortened carbon nanotube architectures on a silicon (100) substrate by direct chemical anchoring. The growth mechanism of the structures is clearly an initial attachment of nanotubes which become nucleation sites for the growth of large bundles. Compared to other techniques, this new technique has several advantages including the low temperature involved and the possibility for further modification. Electrochemistry using the new interface demonstrates excellent conductivity to the substrate meaning this approach has numerous potential applications. The attachment of the SWCNTs directly to the silicon surface provides a simple and new avenue for the fabrication and development of silicon-based electrochemical and bio-electrochemical sensors, solar cells and nanoelectronic devices using further surface modification.

Acknowledgements

JY would like to thank Flinders University for scholarship funding. Thanks also to Dr Claire Lenehan for many helpful discussions regarding the fluorescence behaviour of the nanotube systems. Thanks to Flinders University for funding through the small grants scheme.

References

1 S. Iijima and T. Ichihashi, *Nature*, 1993, **363**, 603–605.
2 D. S. Bethune, C. H. Kiang, M. S. Devries, G. Gorman, R. Savoy, J. Vazquez and R. Beyers, *Nature*, 1993, **363**, 605–607.
3 W. A. Deheer, W. S. Bacsa, A. Chatelain, T. Gerfin, R. Humphreybaker, L. Forro and D. Ugarte, *Science*, 1995, **268**, 845–847.
4 S. S. Fan, M. G. Chapline, N. R. Franklin, T. W. Tombler, A. M. Cassell and H. J. Dai, *Science*, 1999, **283**, 512–514.
5 L. B. Zhu, Y. Y. Sun, D. W. Hess and C. P. Wong, *Nano Lett.*, 2006, **6**, 243–247.
6 M. S. Jung, Y. K. Ko, D. H. Jung, D. H. Choi, H. T. Jung, J. N. Heo, B. H. Sohn, Y. W. Jin and J. Kim, *Appl. Phys. Lett.*, 2005, **87**.
7 S. S. Wong, E. Joselevich, A. T. Woolley, C. L. Cheung and C. M. Lieber, *Nature*, 1998, **394**, 52–55.
8 S. S. Wong, J. D. Harper, P. T. Lansbury and C. M. Lieber, *J. Am. Chem. Soc.*, 1998, **120**, 603–604.
9 S. S. Wong, A. T. Woolley, E. Joselevich, C. L. Cheung and C. M. Lieber, *J. Am. Chem. Soc.*, 1998, **120**, 8557–8558.
10 S. J. Tans, M. H. Devoret, H. J. Dai, A. Thess, R. E. Smalley, L. J. Geerligs and C. Dekker, *Nature*, 1997, **386**, 474–477.
11 M. Bockrath, D. H. Cobden, P. L. McEuen, N. G. Chopra, A. Zettl, A. Thess and R. E. Smalley, *Science*, 1997, **275**, 1922–1925.
12 S. J. Tans, A. R. M. Verschueren and C. Dekker, *Nature*, 1998, **393**, 49–52.
13 P. G. Collins, A. Zettl, H. Bando, A. Thess and R. E. Smalley, *Science*, 1997, **278**, 100–103.
14 M. S. Fuhrer, J. Nygard, L. Shih, M. Forero, Y. G. Yoon, M. S. C. Mazzoni, H. J. Choi, J. Ihm, S. G. Louie, A. Zettl and P. L. McEuen, *Science*, 2000, **288**, 494–497.
15 X. L. Liu, S. Han and C. W. Zhou, *Nano Lett.*, 2006, **6**, 34–39.
16 C. Liu, Y. Y. Fan, M. Liu, H. T. Cong, H. M. Cheng and M. S. Dresselhaus, *Science*, 1999, **286**, 1127–1129.
17 P. Chen, X. Wu, J. Lin and K. L. Tan, *Science*, 1999, **285**, 91–93.
18 G. L. Che, B. B. Lakshmi, E. R. Fisher and C. R. Martin, *Nature*, 1998, **393**, 346–349.
19 R. H. Baughman, C. X. Cui, A. A. Zakhidov, Z. Iqbal, J. N. Barisci, G. M. Spinks, G. G. Wallace, A. Mazzoldi, D. De Rossi, A. G. Rinzler, O. Jaschinski, S. Roth and M. Kertesz, *Science*, 1999, **284**, 1340–1344.
20 J. Kong, N. R. Franklin, C. W. Zhou, M. G. Chapline, S. Peng, K. J. Cho and H. J. Dai, *Science*, 2000, **287**, 622–625.
21 P. G. Collins, K. Bradley, M. Ishigami and A. Zettl, *Science*, 2000, **287**, 1801–1804.
22 D. H. Jung, B. H. Kim, Y. K. Ko, M. S. Jung, S. Jung, S. Y. Lee and H. T. Jung, *Langmuir*, 2004, **20**, 8886–8891.
23 Z. F. Liu, Z. Y. Shen, T. Zhu, S. F. Hou, L. Z. Ying, Z. J. Shi and Z. N. Gu, *Langmuir*, 2000, **16**, 3569–3573.
24 P. M. Ajayan, *Chem. Rev.*, 1999, **99**, 1787–1800.
25 Z. F. Ren, Z. P. Huang, D. Z. Wang, J. G. Wen, J. W. Xu, J. H. Wang, L. E. Calvet, J. Chen, J. F. Klemic and M. A. Reed, *Appl. Phys. Lett.*, 1999, **75**, 1086–1088.
26 Z. F. Ren, Z. P. Huang, J. W. Xu, J. H. Wang, P. Bush, M. P. Siegal and P. N. Provencio, *Science*, 1998, **282**, 1105–1107.
27 J. J. Gooding, R. Wibowo, J. Q. Liu, W. R. Yang, D. Losic, S. Orbons, F. J. Mearns, J. G. Shapter and D. B. Hibbert, *J. Am. Chem. Soc.*, 2003, **125**, 9006–9007.
28 P. Diao and Z. F. Liu, *J. Phys. Chem. B*, 2005, **109**, 20906–20913.
29 D. Chattopadhyay, I. Galeska and F. Papadimitrakopoulos, *J. Am. Chem. Soc.*, 2001, **123**, 9451–9452.
30 D. Losic, J. G. Shapter and J. J. Gooding, *Electrochem. Commun.*, 2001, **3**, 722–726.
31 D. Losic, J. G. Shapter and J. J. Gooding, *Langmuir*, 2001, **17**, 3307–3316.
32 P. Diao, Z. F. Liu, B. Wu, X. L. Nan, J. Zhang and Z. Wei, *ChemPhysChem*, 2002, **3**, 898–901.
33 Z. Chen, Y. L. Yang, Z. Y. Wu, G. Luo, L. M. Xie, Z. F. Liu, S. J. Ma and W. L. Guo, *J. Phys. Chem. B*, 2005, **109**, 5473–5477.
34 F. Patolsky, Y. Weizmann and I. Willner, *Angew. Chem., Int. Ed.*, 2004, **43**, 2113–2117.
35 L. Sheeney-Haj-Khia, B. Basnar and I. Willner, *Angew. Chem., Int. Ed.*, 2005, **44**, 78–83.
36 E. Delamarche, B. Michel, H. Kang and C. Gerber, *Langmuir*, 1994, **10**, 4103–4108.
37 A. B. Horn, D. A. Russell, L. J. Shorthouse and T. R. E. Simpson, *J. Chem. Soc., Faraday Trans.*, 1996, **92**, 4759–4762.
38 M. H. Schoenfisch and J. E. Pemberton, *J. Am. Chem. Soc.*, 1998, **120**, 4502–4513.
39 F. P. Zamborini and R. M. Crooks, *Langmuir*, 1998, **14**, 3279–3286.
40 M. S. Jung, S. O. Jung, D. H. Jung, Y. K. Ko, Y. W. Jin, J. Kim and H. T. Jung, *J. Phys. Chem. B*, 2005, **109**, 10584–10589.
41 J. Yu, D. Losic, M. Marshall, T. Böcking, J. J. Gooding and J. G. Shapter, *Soft Matter*, 2006, 1081–1088.
42 J. M. Buriak, *Chem. Rev.*, 2002, **102**, 1271–1308.
43 G. F. Cerofolini, G. Arena, C. M. Camalleri, C. Galati, S. Reina, L. Renna and M. D., *Nanotechnology*, 2005, **16**, 1040–1047.
44 X. C. Wu, A. M. Bittner and K. Kern, *Adv. Mater.*, 2004, **16**, 413–417.
45 X. C. Wu, A. M. Bittner and K. Kern, *Langmuir*, 2002, **18**, 4984–4988.
46 J. F. Moulder, W. F. Stickle, P. E. Sobol and K. D. Bomben, *Handbook of X-ray Photoelectron Spectroscopy*, Physical Electronics Division, Perkin-Elmer Corporation, Eden Prairie, MN, USA, 1992.
47 K. M. Roth, A. A. Yasseri, Z. M. Liu, R. B. Dabke, V. Malinovskii, K. H. Schweikart, L. H. Yu, H. Tiznado, F. Zaera, J. S.

Lindsey, W. G. Kuhr and D. F. Bocian, *J. Am. Chem. Soc.*, 2003, **125**, 505–517.
48 M. R. Linford, P. Fenter, P. M. Eisenberger and C. E. D. Chidsey, *J. Am. Chem. Soc.*, 1995, **117**, 3145–3155.
49 R. Boukherroub, S. Morin, F. Bensebaa and D. D. M. Wayner, *Langmuir*, 1999, **15**, 3831–3835.
50 T. I. T. Okpalugo, P. Papakonstantinou, H. Murphy, J. McLaughlin and N. M. D. Brown, *Carbon*, 2005, **43**, 153–161.
51 J. Zhang, H. L. Zou, Q. Qing, Y. L. Yang, Q. W. Li, Z. F. Liu, X. Y. Guo and Z. L. Du, *J. Phys. Chem. B*, 2003, **107**, 3712–3718.
52 D. B. Mawhinney, V. Naumenko, A. Kuznetsova, J. T. Yates, J. Liu and R. E. Smalley, *J. Am. Chem. Soc.*, 2000, **122**, 2383–2384.
53 A. Chou, T. Bocking, N. K. Singh and J. J. Gooding, *Chem. Commun.*, 2005, 842–844.
54 T. Hemraj-Benny, S. Banerjee and S. S. Wong, *Chem. Mater.*, 2004, **16**, 1855–1863.
55 A. Jorio, M. A. Pimenta, A. G. Souza, R. Saito, G. Dresselhaus and M. S. Dresselhaus, *New J. Phys.*, 2003, **5**, 139. 131–139.117.
56 M. S. Dresselhaus and P. C. Eklund, *Adv. Phys.*, 2000, **49**, 705–814.
57 M. A. Pimenta, A. Marucci, S. A. Empedocles, M. G. Bawendi, E. B. Hanlon, A. M. Rao, P. C. Eklund, R. E. Smalley, G. Dresselhaus and M. S. Dresselhaus, *Phys. Rev. B*, 1998, **58**, 16016–16019.
58 E. Anglaret, N. Bendiab, T. Guillard, C. Journet, G. Flamant, D. Laplaze, P. Bernier and J. L. Sauvajol, *Carbon*, 1998, **36**, 1815–1820.
59 Y. F. Lian, Y. Maeda, T. Wakahara, T. Akasaka, S. Kazaoui, N. Minami, N. Choi and H. Tokumoto, *J. Phys. Chem. B*, 2003, **107**, 12082–12087.
60 G. Eres, A. A. Kinkhabwala, H. T. Cui, D. B. Geohegan, A. A. Puretzky and D. H. Lowndes, *J. Phys. Chem. B*, 2005, **109**, 16684–16694.
61 Y. Chen and J. Yu, *Appl. Phys. Lett.*, 2005, **87**.
62 R. Krishnan, H. Q. Nguyen, C. V. Thompson, W. K. Choi and Y. L. Foo, *Nanotechnology*, 2005, **16**, 841–845.
63 Y. F. Mei, X. L. Wu, X. F. Li, X. M. Bao, X. Z. Wang, Z. Hu and G. G. Siu, *J. Cryst. Growth*, 2003, **255**, 414–418.
64 H. Ago, S. Imamura, T. Okazaki, T. Saitoj, M. Yumura and M. Tsuji, *J. Phys. Chem. B*, 2005, **109**, 10035–10041.
65 M. J. O'Connell, S. M. Bachilo, C. B. Huffman, V. C. Moore, M. S. Strano, E. H. Haroz, K. L. Rialon, P. J. Boul, W. H. Noon, C. Kittrell, J. P. Ma, R. H. Hauge, R. B. Weisman and R. E. Smalley, *Science*, 2002, **297**, 593–596.
66 A. Hartschuh, H. N. Pedrosa, L. Novotny and T. D. Krauss, *Science*, 2003, **301**, 1354–1356.
67 S. M. Bachilo, M. S. Strano, C. Kittrell, R. H. Hauge, R. E. Smalley and R. B. Weisman, *Science*, 2002, **298**, 2361–2366.
68 J. E. Berlier, A. Rothe, G. Buller, J. Bradford, D. R. Gray, B. J. Filanoski, W. G. Telford, S. Yue, J. X. Liu, C. Y. Cheung, W. Chang, J. D. Hirsch, J. M. Beechem, R. P. Haugland and R. P. Haugland, *J. Histochem. Cytochem.*, 2003, **51**, 1699–1712.
69 M. Roederer, A. B. Kantor, D. R. Parks and L. A. Herzenberg, *Cytometry*, 1996, **24**, 191–197.
70 L. T. Canham, *Appl. Phys. Lett.*, 1990, **57**, 1046–1048.
71 B. D. Rowsell and J. G. C. Veinot, *Nanotechnology*, 2005, **16**, 732–736.
72 A. G. Cullis, L. T. Canham and P. D. J. Calcott, *J. Appl. Phys.*, 1997, **82**, 909–965.
73 P. J. Moyer, A. Pridmore, T. Martin, J. Schmidt, T. Hasche, L. Eng and J. L. Gole, *Appl. Phys. Lett.*, 2000, **76**, 2683–2685.
74 R. S. Nicholson, *Analytical Chemistry*, 1965, **37**, 1351–1355.
75 A. J. Bard and L. R. Faulkner, *Electrochemical Methods: Fundamentals and Applications*, Wiley, New York, 2nd edn, 2000.
76 T. Kuwana, D. E. Bublitz and G. Hoh, *J. Am. Chem. Soc.*, 1960, **82**, 5811–5817.
77 M. Noel, V. Suryanarayanan and R. Santhanam, *Electroanalysis*, 2000, **12**, 1039–1045.
78 S. Haymond, G. T. Babcock and G. M. Swain, *Electroanalysis*, 2003, **15**, 249–253.

